Spectrally-resolved measurement of concentrated light distributions for Fresnel lens concentrators

P. Besson,[1,5] P. McVey White,[2,6] C. Dominguez,[3] P. Voarino,[1] P. Garcia-Linares,[1] M. Lemiti,[4] H. Schriemer,[2] K. Hinzer,[2] and M. Baudrit[1]

[1] *CEA-LITEN, LCPV, INES, Le Bourget du Lac, France*
[2] *SUNLAB, Centre for Research in Photonics, University of Ottawa, Ottawa, Canada*
[3] *Instituto de Energía Solar, Universidad Politécnica de Madrid, Madrid, Spain*
[4] *University of Lyon, Lyon Institute of Nanotechnology, National Institute of Applied Sciences of Lyon, Villeurbanne, France*
[5] *pierre.besson@cea.fr*
[6] *pwhit032@uottawa.ca*

Abstract: A test method that measures spectrally resolved irradiance distribution for a concentrator photovoltaic (CPV) optical system is presented. In conjunction with electrical *I-V* curves, it is a means to visualize and characterize the effects of chromatic aberration and nonuniform flux profiles under controllable testing conditions. The indoor characterization test bench, METHOD (Measurement of Electrical, Thermal and Optical Devices), decouples the temperatures of the primary optical element (POE) and the cell allowing their respective effects on optical and electrical performance to be analysed. In varying the temperature of the POE, the effects on electrical efficiency, focal distance, spectral sensitivity, acceptance angle and multi-junction current matching profiles can be quantified. This work presents the calibration procedures to accurately image the spectral irradiance distribution of a CPV system and a study of system behavior over lens temperature.

OCIS codes: (350.6050) Solar energy; (120.0120) Instrumentation, measurement, and metrology; (040.5350) Photovoltaic; (220.1770) Concentrators.

References and links

1. Fraunhofer ISE, Soitec, CEA-Leti, "New world record for solar cell efficiency at 46%: French-German cooperation confirms competitive advantage of European photovoltaic industry," [Press Release], Freiburg (2014). http://www.ise.fraunhofer.de/en/press-and-media/press-releases/press-releases-2014/new-world-record-for-solar-cell-efficiency-at-46-percent.
2. Fraunhofer ISE, Soitec, CEA-Leti, "Four-junction solar cell developped using Soitec's expertise in semiconductor materials sets new efficiency record of 38.9% for CPV module," [Press Release], Grenoble (2015). http://www.soitec.com/en/news/press-releases/article-1737.
3. J. Haysom, O. Jafarieh, H. Anis, K. Hinzer, and D. Wright, "Learning curve analysis of concentrated photovoltaic systems," Prog. Photovolt. Res. Appl. **23**(11), 1678–1686 (2015).
4. P. Sharma, A. W. Walker, J. F. Wheeldon, K. Hinzer, and H. Schriemer, "Enhanced efficiencies for high concentration, multijunction PV systems by optimizing grid spacing under nonuniform illumination," Int. J. Photoenergy **2014**, 1–7 (2014).
5. R. Herrero, M. Victoria, S. Askins, C. Domínguez, I. Antón, G. Sala, and J. Berrios, "Indoor characterization of multijunction solar cells under non uniform light patterns," in *CPV6 Conf. Proc.* (Amer Inst. Physics, 2010), pp. 36–38.
6. S. Kurtz, D. J. Friedman, and J. M. Olson, "The effect of chromatic aberrations on two-junction, two-terminal, devices on a concentrator system," in *Conf. Record of the 24th IEEE PVSC* (IEEE, 1994), pp. 1791–1794.
7. P. Espinet-González, R. Mohedano, I. García, P. Zamora, I. Rey-Stolle, P. Benitez, C. Algora, A. Cvetkovic, M. Hernández, J. Chaves, J. C. Miñano, and Y. Li, "Triple-junction solar cell performance under fresnel-based concentrators taking into account chromatic aberration and off-axis operation," in *CPV8 Conf. Proc.* (Amer. Inst. Physics, 2012), pp. 81–85.

#251636 Received 15 Oct 2015; revised 20 Nov 2015; accepted 22 Nov 2015; published 7 Jan 2016

8. M. Victoria, R. Herrero, C. Domínguez, I. Antón, S. Askins, and G. Sala, "Characterization of the spatial distribution of irradiance and spectrum in concentrating photovoltaic systems and their effect on multi-junction solar cells," Prog. Photovolt. Res. Appl. **21**(3), 308–318 (2013).
9. S. Askins, M. Victoria, R. Herrero, and C. Domínguez, "Optimizing CPV systems for thermal and spectral tolerance," in *Proc. 27th EU PVSEC* (2012), pp. 194–198.
10. P. Benítez, J. C. Miñano, P. Zamora, R. Mohedano, A. Cvetkovic, M. Buljan, J. Chaves, and M. Hernández, "High performance Fresnel-based photovoltaic concentrator," Opt. Express **18**(1), A25–A40 (2010).
11. I. Antón, C. Dominguez, M. Victoria, R. Herrero, S. Askins, and G. Sala, "Characterization capabilities of solar simulators for concentrator photovoltaic modules," Jpn. J. Appl. Phys. **51**(10S), 1–4 (2012).
12. C. Domínguez, I. Antón, G. Sala, and S. Askins, "Current-matching estimation for multijunction cells within a CPV module by means of component cells," Prog. Photovolt. Res. Appl. **21**(7), 1478–1488 (2013).
13. W. Smith, *Modern Optical Engineering; The Design of Optical Systems, 3rd Edition* (McGraw-Hill, 2000).
14. H. P. Baltes, *Inverse Scattering Problems in Optics* (Springer-Verlag Berlin Heidelberg, 1980).
15. M. Victoria, "SOE for Fresnel lenses," in *New Concepts and Techniques for the Development of High-Efficiency Concentrating Photovoltaic Modules* (Academic, Universidad politecnica de Madrid, 2014), pp. 48–49.
16. T. Hornung, M. Steiner, and P. Nitz, "Estimation of the influence of Fresnel lens temperature on energy generation of a concentrator photovoltaic system," Sol. Energy Mater. Sol. Cells **99**, 333–338 (2012).
17. T. Hornung, A. Bachmaier, P. Nitz, A. Gombert, A. W. Bett, R. D. McConnell, G. Sala, and F. Dimroth, "Temperature dependent measurement and simulation of Fresnel lenses for concentrating photovoltaics," in *CPV6 Conf. Proc.* (Amer Inst Physics, 2010), pp. 85–89.
18. R. Mohedano, P. Benitez, P. Zamora, J. C. Miñano, J. Mendes, A. Cvetkovic, J. Vilaplana, M. Hernandez, J. Chaves, and G. Biot, "Ventana power train features and performance," in *CPV9 AIP Conf. Proc.* (Amer. Inst. Physics, 2013), pp. 176–179.
19. I. Garcia, P. Espinet-Gonzalez, I. Rey-Stolle, E. Barrigon, C. Algora, F. Dimroth, S. Kurtz, G. Sala, and A. W. Bett, "Extended triple-junction solar cell 3d distributed model: application to chromatic aberration-related losses," in *CPV7 Conf. Proc.* (Amer. Inst. Physics, 2011), pp. 13–16.

1. Introduction

A multi-junction solar cell (MJSC) is a series-interconnected stack of semiconductors where each harvests a different band of the solar spectrum to more efficiently transform sunlight into electricity. Concentrator photovoltaics (CPV) systems then leverage inexpensive optical components to concentrate light onto these highly efficient small area cells. World record cell and module efficiencies of 46% and 38.9%, respectively [1, 2], have been achieved using MJSCs under concentration. With the increase in global cumulative deployment volume and a consistent decrease in system cost, CPV systems now cost as little as 1 $/W, and the costs continue to fall faster than for traditional photovoltaics systems [3]. However, the necessary use of concentrating optics may result in chromatic aberration and a nonuniform illumination profile across the MJSC, thus reducing its electrical performance. Spatial non-uniformity increases the losses due to cell series resistance [4,5]. Spectral inhomogeneities will increase losses due to local subcell current limitations [6]. The inhomogeneity of irradiance and spectrum are given by the optical design, but these properties are highly sensitive to other factors like the distance between the primary optical element (POE) and the receiver, the POE temperature [7, 8], or the presence of a secondary optical element (SOE) [9]. Thus, these factors can be used to tune the inhomogeneity of intensity and spectrum.

An indoor optical-electrical measurement methodology has been developed to characterize the spatial and spectral nonuniformity produced by CPV optics. CCD or CMOS image sensors are commonly used to measure the light intensity distribution cast by the optics in a CPV system [6]. The current generation profile of a cell can be studied through images taken at different wavelengths and, in conjunction with electrical measurements, allows in depth analysis of single-lens module behavior under various conditions. We first present the test bench instrumentation and the calibration procedures for spectral imaging. Next, the top and middle subcell currents are calculated from the spectrally resolved images and compared to their isotype meaurements. Finally, the impact of primary lens temperature is demonstrated by comparing the opto-electrical performance of two systems: (1) a silicone on glass Fresnel lens without a secondary; and (2) a PMMA, four Fresnel-Köhler (4FK) lobe system [10].

#251636 Received 15 Oct 2015; revised 20 Nov 2015; accepted 22 Nov 2015; published 7 Jan 2016

2. Experimental setup

The METHOD testbench, shown schematically in Fig. 1, allows both optical and electrical characterization of CPV systems. This experimental technique is realized with a HELIOS solar flash simulator, an indoor solar simulator that produces direct normal irradiance on a CPV system and uses reference sensors to monitor both the spectrum and concentration through a 2 ms flash from a xenon bulb [11]. The light is collimated using a 2 meters diameter parabolic mirror on the testbench. It is comprised of an *imaging module*, an *electrical module*, and a *reference measurements* section. A thermal chamber encloses the POE with solar glass on both the front and rear surfaces, allowing light to pass through, which decouples the temperature of lens and cell. It is mounted on a positioning stage that can be moved to cast the light from the POE either on the imaging module or the electrical module. The POE can be heated from 25°C to 60°C by two compact heaters installed on either side of the thermal chamber. The thermal uniformity of the POE is ± 1C° under cooling at a rate of 1C°/minute.

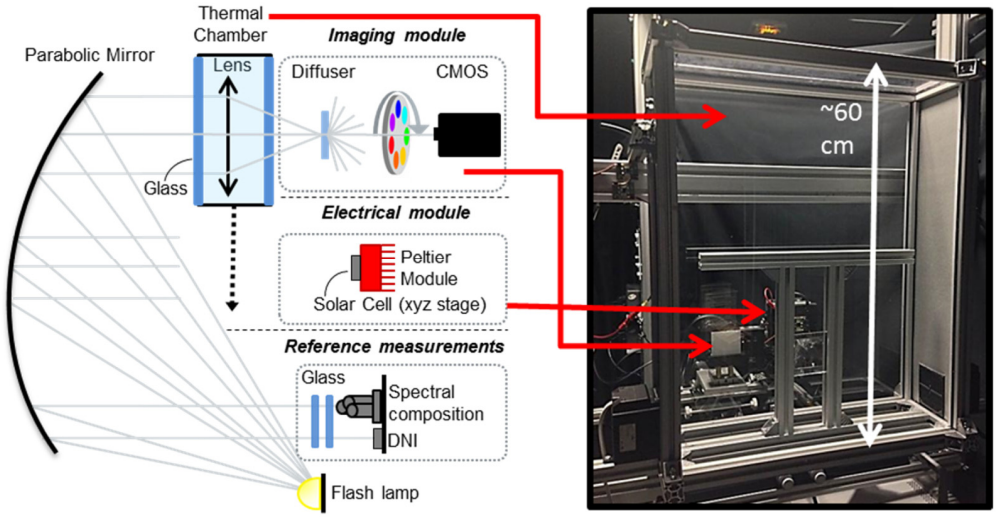

Fig. 1. Schematic of the instrumentation used in the METHOD testbench.

The *imaging module* consists of an opal diffuser, a filter wheel with twelve 50 nm (full width half maximum) bandpass filters, and a near infrared (NIR) CMOS camera. This type of sensor allows acquiring signal for the spectral region 350-1100nm. The collimated beam from the xenon flash is focused by the POE onto the diffuser located at the focal plane of the camera. This location corresponds to the position of the MJSC under electrical measurement. A diffuser is used since its near-Lambertian response allows a common focal plane to be established for all spectral ranges, while capturing the full chromatic aberration of the POE. An opal diffuser was selected since it has a better lambertian behavior in the visible spectrum over a typical ground glass diffuser. The filters were selected to divide the intensity profile into twelve separate spectral bands in order to fully characterize top and middle subcells and to fit the 350 to 1100 nm spectral response of the camera. The central wavelengths of the filters range from 400 nm to 950 nm, in 50 nm increments. The camera captures a 12.8 x 10 mm image with a resolution of 1280 x 1024 pixels (1 pixel = 10 μm^2). In order to capture the image at the correct time within a pulse, an external photodetector is used to trigger the camera. The output of the Imaging System is a set of 12 images, acquired within 20 seconds.

Spectral respone of the camera and filters limits the *imaging module* to only study the top and middle subcells of a triple-junction cell. This has a limited impact for conventional CPV module, using lattice-matched triple-junction cells. However, bottom subcell of such device

#251636 Received 15 Oct 2015; revised 20 Nov 2015; accepted 22 Nov 2015; published 7 Jan 2016

are known to produce an excess of photogenerated current under outdoor conditions. Therefore, the top and middle subcells will limit the total photogenerated current since the subcells are connected in series. Moreover, dispersion of CPV optical materials is relatively low for wavelengths above 1100nm, and light distribution seen by the bottom subcell is similar to the middle subcell. Results presented in this work are therefore considered for top and middle subcells.

The *electrical module* consists of a MJSC mounted on a Peltier module to maintain a stable cell temperature from 20°C to 100°C with 0.1°C precision. The Peltier module is fixed on an *x-y-z* translation stage to optimize or vary the cell position with respect to the POE. Since the incident spectrum varies across the temporal profile of the flash (and from flash to flash) due to changing lamp temperature, the spectral composition of the incident light is measured by individual subcell isotypes [11, 12]. To link the measurements of the reference instruments and the device under test, it is sufficienty to place two panels of the same glass that encloses the thermal chamber in front of the reference measurement instruments. This allows the METHOD testbench to be used to study the effects of POE temperature, or cell position, on the electrical performance and irradiance profile of a given CPV system.

3. Spectral irradiance profile measurement technique

Here we discuss how raw images from the Imaging System are converted into spectral band irradiance profiles and how the generated currents of top and middle subcells are obtained. The calibration procedure to obtain a spectrally resolved irradiance distribution is first described, then its validation with electrical measurements.

3.1. Calibration procedure to obtain the spectrally resolved irradiance distribution

In order to quantify the spatial dependence of each 50 nm spectral irradiance band across the MJSC, the CMOS camera images must be calibrated. There are four calibration factors that must be applied to the CMOS signal to transform pixel counts to a final irradiance value. Each filter and pixel are represented by index *i* and coordinate system x,y, respectively. A dark image is taken to account for thermal noise, which is subtracted from the raw image measured under illumination. The resulting signal $S_i(x,y)$ is then calibrated to produce a spectral irradiance $F_i(x,y)$, in W/m^2/nm, as

$$F_i(x,y) = S_i(x,y) \Big/ C_i^{tot}(x,y) \tag{1}$$

where

$$C_i^{tot}(\mathrm{x,y}) = C_i^{pow} \cdot C_i^{unif}(\mathrm{x,y}) \cdot C_i^{lin} \cdot C_i^{adj} \tag{2}$$

is the total calibration factor comprised of C_i^{pow}, which addresses the conversion from counts to W/m^2/nm; $C_i^{unif}(x,y)$, which accounts for any spatially non-uniform response across the image sensor; C_i^{lin}, which corrects for nonlinearity in camera response; and C_i^{adj}, which adjusts for the actual filter response.

The first factor to apply, C_i^{pow}, converts pixel counts to irradiance values. The total irradiance seen by the camera was determined by placing a calibrated source a fixed distance from the diffuser and integrating its known spectrum with the known filter transmittance for each filter. Since diffuser transmission depends on incident angle, this calibration was done over all relevant angles and an appropriate average then detemined. Figure 2 shows the extracted calibration constants for each filter, denoted by its central wavelength, at six angles ranging from normal incidence to 25°, shown sequentially by the color-coded bar graph. In

#251636 Received 15 Oct 2015; revised 20 Nov 2015; accepted 22 Nov 2015; published 7 Jan 2016

reference to the dark blue bars (normal incidence) in Fig. 2, the calibration constant of the filters with a central wavelengths above 700 nm begin to diverge from the off-axis results as the lambertian behavior of the diffuser increasingly breaks down due to increased forward scattering [13,14]. Therefore, the forward scattered light in this frequency range will result in a misrepresentative sensor reading and a false calibration factor. Nevertheless this effect can be observed for a limited number of ray angles, as observed on Fig. 2, and we will neglect the forward scattered component at long wavelengths in our approach. The remainder of the data show variations on the order of 10%, which implies that any final calibration factor will not be sensitive to the angular averaging procedure. For convenience, we chose to use the 15° results as representative of average calibration factors since this is close to the median angle of typical Fresnel concentrators under consideration [15].

The second factor, $C_i^{unif}(x,y)$, accounts for any spatially non-uniform response across the image sensor. Ideally, the camera's digital response from each pixel will be the same for a given illumination, but in practice the response across the image sensor varys by about 5%. To determine the correction factor for each pixel, uniform illumination on the diffuser across the camera's field of view was achieved with a calibration lamp. The correction factor for each pixel was determined by dividing each pixel by the mean of the image.

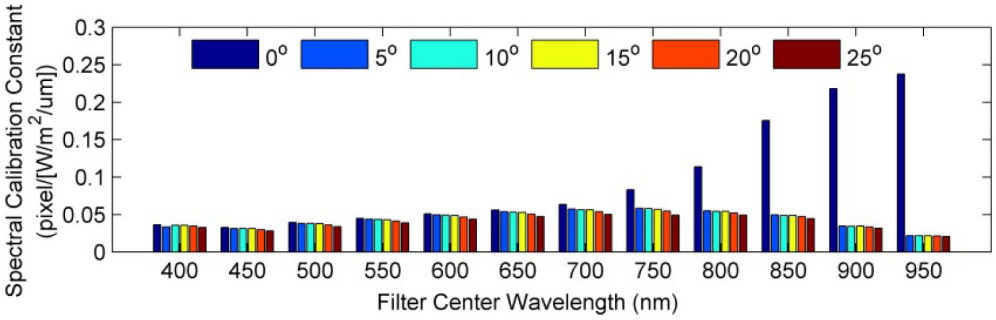

Fig. 2. Dependence of the spectral calibration constant on incident angle to the diffuser for each filter.

The third correction factor, C_i^{lin}, accounts for any non-linear response of the electronics to variations in light intensity. Ideally, the response of the sensor would be a signal directly proportional to the light incident on each pixel, but the electronics introduce a slight nonlinear response, up to 2%, particularly near the noise floor and near saturation. Therefore, characterizing the linearity of the signal for each filter has been calculated with a calibrated lamp, varying the intensity at the sensor through adjusting the integration times of the camera.

The final correction factor, C_i^{adj}, accounts for non-ideal filter response and any spectral overlap, since the initial presumption is 100% transmission over contiguous filter bins. The final goal is to reproduce spectral irradiance on the diffuser for spectral band of 50 nm. However, the transmittance of the filters is not 100% over their full range and the result is a non-perfect rectangular transmission of light and a slight overlaps between bands. Therefore, a simple correction is applied to account for this phenomenon: for a Xenon lamp spectrum equivalent to the spectrum AM1.5D, the transmitted light power ratio between ideal and real filters are calculated. These values are then applied as correction factors.

The spectrally resolved irradiance distirbution seen by a MJSC in a CPV system can now be calculated from the images acquired through the *imaging module*. In Fig. 3, the 2-dimensional cross section plot of the corrected irradiance profiles for a silicone on glass POE can be viewed for a 5x5 mm^2 area on the diffuser. The cross-section is taken for a central line of the spot. All twelve images are acquired at a fixed diffuser to POE distance. For clarity, only selected wavelengths are plotted since there is little difference in profiles at higher

#251636 Received 15 Oct 2015; revised 20 Nov 2015; accepted 22 Nov 2015; published 7 Jan 2016

wavelenghts. The profiles illustrate the wavelength dependence due to chromatic aberration of the POE. This phenomenon can be seen when comparing the profiles at 950 nm to 400 nm, where the longer wavelengths are more tightly focused than the lower wavelengths. The asymmetry of the profiles can be related to the imaging properties of the POE. Since the source is a xenon bulb and not a uniform light source, its shape is imaged onto the diffuser.

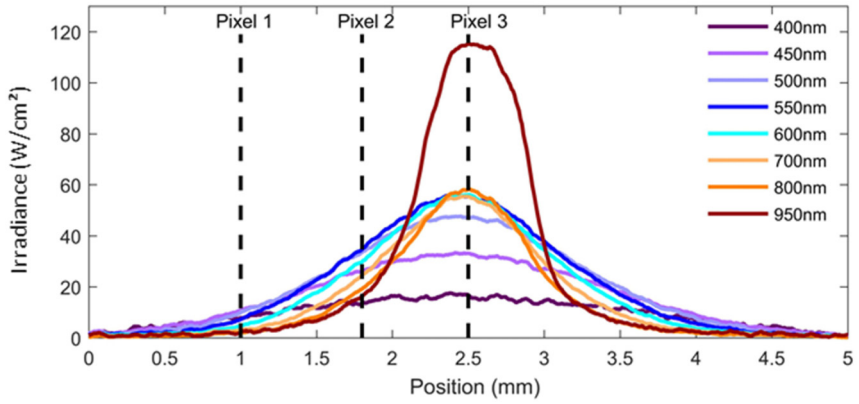

Fig. 3. Cross-sections of the intensity profile for transmission through each filter.

The irradiance values calculated in Fig. 3 are used to generate a spectrum of 50 nm resolution for each pixel (25M points on the 5 x 5 mm^2 area). To illustrate this, the spectral irradiance of three separate pixels showing a different spectral balance due to the chromatic aberration on the diffuser, or as seen by a MJSC, are represented in Fig. 4. The pixels are chosen on the edge of the beam profile. The spectra are normalized by their power to better compare their spectral composition. Due to chromatic aberration, at the edge of the profile (pixel 1), the spectrum is strongly blue shifted. As we move toward the centre of the beam, the spectrum becomes more balanced (pixel 2), and at the beam centre (pixel 3), the spectrum becomes red-rich.

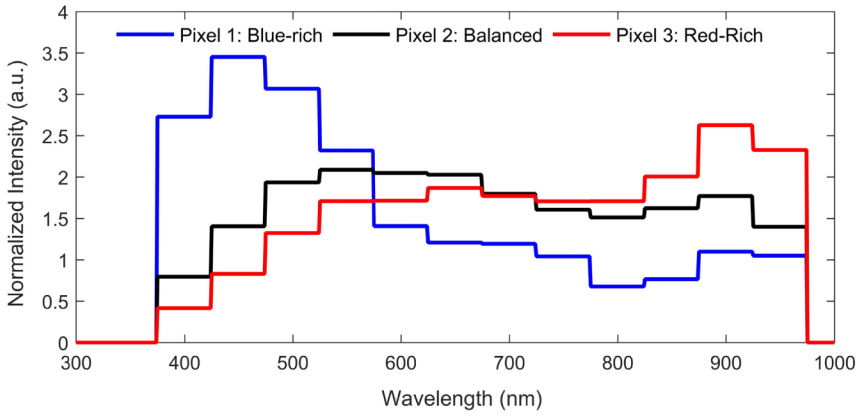

Fig. 4. Spectral irradiance is represented for 3 positions of the cross-section in Fig. 3. The spectra are normalized to their power under concentration for better comparison.

3.2 Validation of spectral irradiance calculation with electrical measurements

The local subcell current densities, $J_i(x,y)$, of a solar cell can be calculated from the spectrally resolved irradiance obtained by the imaging process as,

#251636 Received 15 Oct 2015; revised 20 Nov 2015; accepted 22 Nov 2015; published 7 Jan 2016

$$J_i(x,y) = \sum_{\lambda} \frac{q\lambda}{hc}.e(\lambda,x,y).EQE_i(\lambda) \quad (3)$$

where EQE_i is the measured external quantum efficiency for each subcell i and $e(\lambda,y,z)$ is the local irradiance at each point density: Then, the short-circuit currents, $I_{sc,i}$, for each subcell can be calculated from the following equation:

$$I_{sc,i} = \sum_{x,y} J_i(x,y).A_{pixel} \quad (4)$$

where A_{pixel} corresponds to the pixel area and x, y are the position on the cell constrained by the total surface area of the cell. We now compare currents calculated from the image profiles to those measured by the top and middle subcell isotypes (5x5 mm^2) of a lattice matched MJSC from Spectrolab. The POE used in this study is a SOG Fresnel lens designed for concentrating the light 500X on a 3 mm diameter cell.

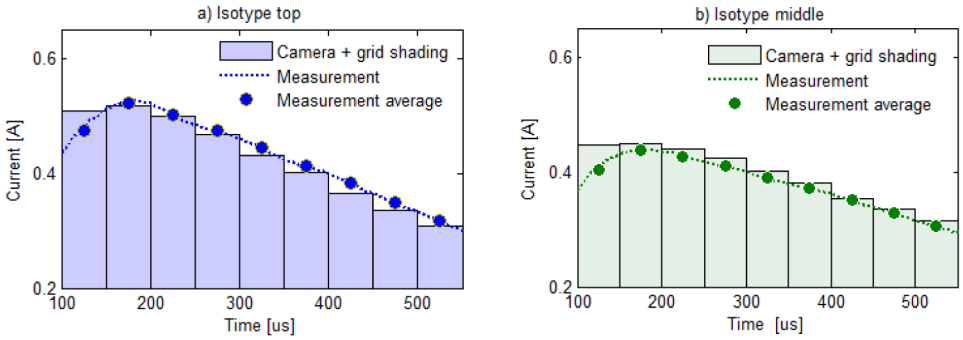

Fig. 5. Comparison of photogenerated currents determined by the mean of spot imaging and from electrical measurements of top (a) and middle isotypes (b). Measure average corresponds to an average on a 50 μs period, equivalent to the integration time used for image acquisition.

The measured short circuit currents of the isotypes are compared to the currents calculated from the spectral images for a given flash, and the data presented in Fig. 5. The integration time of the camera was set to 50 μs and images were captured at different points along the flash. Adding in known grid shading losses of 5%,, we obtain an underestimation of 3% and an overestimation of 2% for the top and middle subcell, respectively. From these results, the forward scattered light of the diffuser for wavelengths greater than 700nm did not introduce a significant increase of calculated middle subcell current. When accounting for the non-flat filter response, angular distribution of incident angles, and diffuser-related issues described, these results are satisfying for the conversion methodology and the lens tested. For other optical concentrators, comparing current measured and calculated can be considered a necessary validation process.

4. Results

In order to illustrate the capabilities of the METHOD test bench, we will first study a SOG lens with a 376X geometrical concentration factor in combination with a 10 x 10 mm^2 Emcore triple-junction cell. The focal distance given by the manufacturer is 285 mm, and there is no SOE.

The first test performed was to generate different spot profiles depending on lens temperatures. Results are presented in Fig. 6 for four temperatures. Current densities are given for a cell I_{SC} corresponding to STC conditions (1000 W/m^2), *i.e.,* 4.2 A at T_{lens} = 20°C. For the sake of simplicity and a better representation of current density evolution with lens temperature, this I_{SC} value is used for calculating current densities at other lens temperatures.

#251636 Received 15 Oct 2015; revised 20 Nov 2015; accepted 22 Nov 2015; published 7 Jan 2016

First, there is an asymmetry in the current density plots. This shape appears because the SOG lens is imaging the toroidal shape of the xenon lamp.The shape is visible depending on spectral range due to the wavelength dependence of the focal distance. However even though its spot shape differs from on-sun conditions, comparable chromatic aberration exists and the spectral non-uniformities caused by the POE on the MJSC can be observed.

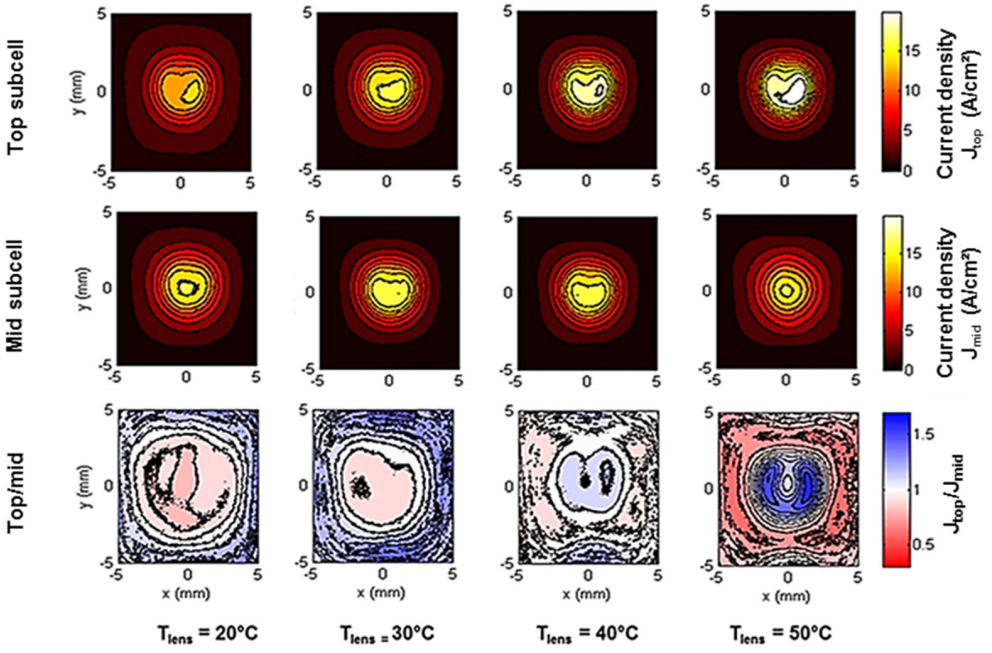

Fig. 6. Top and middle subcells current densities determined with the imaging system, and the resulting J_{top}/J_{mid} ratio showing its dependence on lens temperature for a 376 cm^2 SOG lens focusing light on a 1 cm^2 area. For helping comparisons, J_{sc} values at elevated temperatures are based on normalised values of the current I_{sc} at standard temperature conditions.

Now, we consider the evolution of current densities J_{top} and J_{middle} with POE lens temperature. Values of maximum current densities for both subcells are between 12 and 18 A/cm^2, depending on lens temperature. These values correspond to a peak to average ratio (PAR) between 2.9 and 4.3, respectively. As the POE temperature increases, the PAR of the top subcell current density profile also increases, creating a higher amount of current in the center of the cell. The middle subcell current density, however, remains stable. Due to these different trends, at T_{lens} = 20°C the spatial current density from the top differs only slightly from that of the middle, whereas at T_{lens} = 50°C, the difference is striking. The physical mechanism responsible of the temperature dependence of Fresnel lens is explained in [16,17], and is related to thermal expansion of the optic material. Thermal expansion causes a decrease in the refractive index of the lens, resulting in an increase in focal length. Moreover, the shape of the Fresnel facets is modified leading to a beam shape distortion.

The beam distortion and chromatic aberration is quantified by the temperature evolution of the top to middle subcell current ratio. The observed ratio ranges from 0.85 to 1.15 and from 0.5 to 1.5, for T_{lens} of 20°C and 50°C, respectively. At higher POE temperatures, there is a higher spectral mismatch between the top and middle subcells. Furthermore, there is a difference in the spatial current limitation. In reference to Fig. 6, at T_{lens} = 20°C, the light focused at the center of the cell corresponds to a red-rich spectrum, demonstrating a top subcell current limiting zone. As the temperature is increased, the center of the cell becomes middle-limited due to a blue-rich spectrum. Consequently, this phenomenon has an impact on

#251636 Received 15 Oct 2015; revised 20 Nov 2015; accepted 22 Nov 2015; published 7 Jan 2016

the global current matching of the cell. At T_{lens} of 20°C and 50°C, the observed global J_{top}/J_{mid} ratios are 0.98 and 1.04, respectively. The primary-to-cell distance set by the manufacturer is well adapted for lab conditions for a spectrum equivalent to AM1.5D (SMR = 1) and lens temperature equal to 20°C. However, it is evident that, once the system is subject to changes in POE temperature or incident spectrum, there is a significant impact on performance. In the field, lens temperature and spectrum will vary throughout the day. The optimal cell position may therefore be different than the one determined under STC conditions.

We now compare two fundamentally different devices with respect to lens temperature. Device A is a SOG lens concentrator (~500X) focusing light on a 7 mm^2 Azurspace cell with a circular shape. The POE-cell distance was set to 96mm from the POE, corresponding to an optimized power production at a lens temperature of 25°C. Device B is a PMMA 4FK lobe concentrator [18] corresponding to a fourfold two-stage optical concentrator. It combines a Fresnel lens POE and a refractive SOE, splitting the light into four Köhler channels. The POE-cell distance set by the manufacturer is 260 mm. The geometrical concentration is ~1000 X, defined over 5 x 5 mm^2 illuminated Emcore cell. The *I-V* curves shown in Fig. 7 where taken at 600 W/m^2 with a blue blue-rich spectrum corresponding to an SMR value of 1.1.

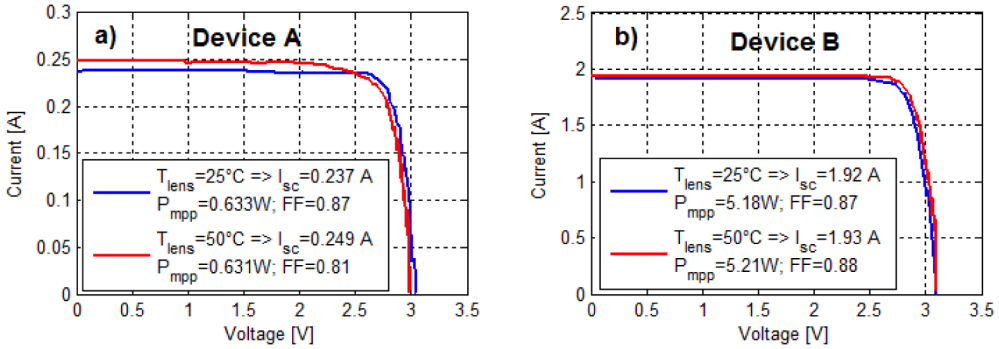

Fig. 7. *I-V* curves of two different concentrator technologies for two lens temperatures. (a) Device A is a single optical element concentrator (SOG lens); and (b) Device B is a 2 stage Fresnel-Köhler concentrator.

Figure 7 shows a difference in electrical performance depending on lens temperature for device A. However, the temperature of the POE minimally affects device B. More specifically, device A has an increase of 5% in the short circuit current at high lens temperature. However, there is a drop in fill factor of 0.87 to 0.81. The variation in terms of efficiency is therefore not significant in this case, and both systems show similar performance in terms of power produced when lens temperature is increased.

To study device behavior, we have performed spot imaging analysis for two extreme lens temperatures. Trigger delay for image acquisition is set up so that *I-V* curve measurement is taken at the same point in the flash. As mentioned in section 3, electrical measurements are used to scale current densities determined with the *imaging module* to the I_{sc} measured on the *I-V* curve. Figure 8 illustrates two parameters of interest: the J_{top}/J_{mid} ratio, and a cross-section of the current density generated by top and middle subcells, normalized by the mean current density for the cell size considered. A cross-section is taken for a central line of the spot. Our first observation concerns the spatial distribution of light intensity. Device A gives a spot with a gaussian profile whereas device B produces a spot with a much more uniform distribution. The absence of an SOE in the case of device A explains such optical behavior, whereas the 4FK optic is known to produce a highly uniform pattern [10,18]. This non-uniformity can be quantified through the maximum value of the normalized current density plot. We will consider this value to be the PAR for the spot. The top subcell PAR values for device A are 3

#251636 Received 15 Oct 2015; revised 20 Nov 2015; accepted 22 Nov 2015; published 7 Jan 2016

and 4, for T_{lens} of 25°C and 50°C, respectively. However, device B presents a flat normalized current density of 1.2 for a central area of 4 x 4 mm^2 side.

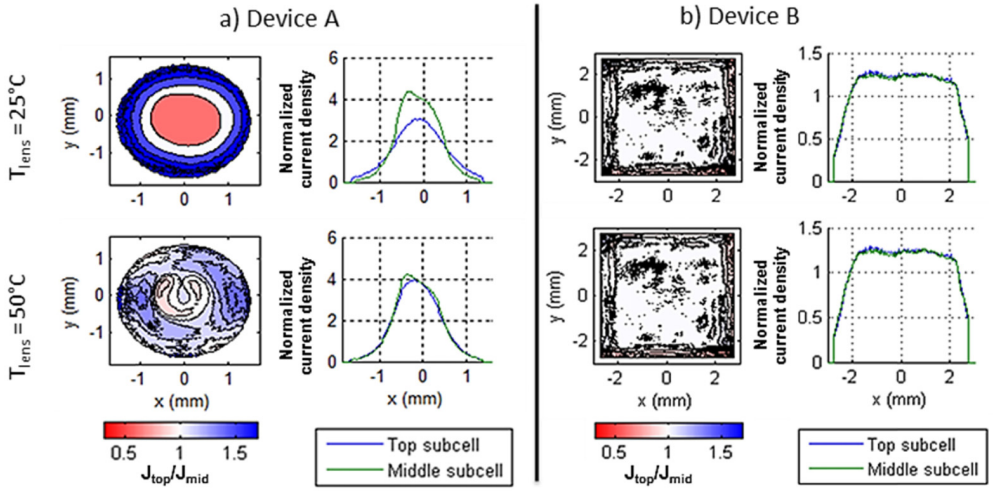

Fig. 8. J_{top}/J_{mid} ratio and the current density normlized by the average value on the cell for a centered cross-section of the spot for 2 different concentrators, (a) Device A, and (b) Device B.

In the case of device A, notable chromatic aberration can be observed. At T_{lens} = 25°C, a red-rich spectrum is focused at the center of the cell, whereas on the edges, the light is blue-rich. The result is a global J_{top}/J_{mid} ratio of 0.92. The normalized current density profiles for the top and middle subcell introduce strong spatial current limitation forcing lateral current flows within the device [19]. For T_{lens} = 50°C, the PAR of the top subcell increases and there is greater balance in the current generation profiles resulting in a global current matching of 0.97. Furthermore, there is a decrease in lateral current flows. The effects that this has on system electrical performance are seen in Fig. 7. At T_{lens} = 50°C, there is an increase in short circuit current due to higher degree of over all current matching between the subcells. Furthermore, with a lower PAR of the limiting subcell at a T_{lens} = 25°C, the fill factor will be higher. The drop in fill factor at higher temperature can be explained by the increase in PAR. As the PAR increases, there will be more current generated in the middle of the subcell resulting in higher series resistance.

In agreement with electrical measurements, the optical behavior of device B is tolerant to changes in POE temperature. Altough less sensitive to temperature (compared to SOG), PMMA's index of refraction still changes with temperature, and so alters the focal distance and spot profile. This change is not significant enough to induce a visible change at the output of the 4FK secondary optic. The POE-SOE combination of device B therefore balances the thermal sensitivity of the POE against chromatic mismatch produced by concentrator misalignments, as shown in [9].

5. Conclusions

A test bench, METHOD, has been presented along with a methodology for measuring the spectrally resolved irradiance distribution of a CPV optical system. The spectral imaging process can be applied to different CPV systems to create current generation profiles to analyze CPV system performance as a function of POE lens temperature. The indoor test bench allows for full independent control of POE and cell temperatures in order to study the CPV performance under the various conditions it will face in the field. Comparing these profiles to electrical measurements of the system under the same conditions can provide

#251636 Received 15 Oct 2015; revised 20 Nov 2015; accepted 22 Nov 2015; published 7 Jan 2016

greater insight into the effect of non-uniform illumination profiles and chromatic aberrations on the cell electrical performance.

Acknowledgments

The author thanks LPI and Soitec for their collaboration and all other partners involved. Partial funding from the European Union's Horizon 2020 research and innovation program within the project CPVMatch under grant agreement No 640873, and Natural Science and Engineering Research Council of Canada (NSERC), are acknowledged. The authors are solely responsible for the content of this work and it only reflects the author's view. The European Commission or any of their agencies are not responsible for any use that may be made of the information it contains.

#251636 Received 15 Oct 2015; revised 20 Nov 2015; accepted 22 Nov 2015; published 7 Jan 2016